ECOLOGY

Enhancing ecosystem productivity and stability with increasing canopy structural complexity in global forests

Xiaoqiang Liu[1,2,3], Yuhao Feng[4], Tianyu Hu[1,2,3], Yue Luo[1,2,3], Xiaoxia Zhao[1,2,3], Jin Wu[5], Eduardo E. Maeda[6,7], Weiming Ju[8], Lingli Liu[1,2,3], Qinghua Guo[4,9], Yanjun Su[1,2,3]*

Forest canopy structural complexity (CSC) plays a crucial role in shaping forest ecosystem productivity and stability, but the precise nature of their relationships remains controversial. Here, we mapped the global distribution of forest CSC and revealed the factors influencing its distribution using worldwide light detection and ranging data. We find that forest CSC predominantly demonstrates significant positive relationships with forest ecosystem productivity and stability globally, although substantial variations exist among forest ecoregions. The effects of forest CSC on productivity and stability are the balanced results of biodiversity and resource availability, providing valuable insights for comprehending forest ecosystem functions. Managed forests are found to have lower CSC but more potent enhancing effects of forest CSC on ecosystem productivity and stability than intact forests, highlighting the urgent need to integrate forest CSC into the development of forest management plans for effective climate change mitigation.

INTRODUCTION

Forest canopy serves as the central hub of carbon and energy exchange between trees and the atmosphere (*1*, *2*). An essential determinant of this exchange process is the intricate arrangement and occupation of canopy elements in three-dimensional space, known as canopy structural complexity (CSC) (*3*, *4*). Forest CSC governs the distribution of light and water within forest canopy (*5*, *6*), thereby exerting a profound influence on crucial functions of forest ecosystems, especially their productivity and stability (*7*–*9*). Against the backdrop of global climate change and forest biodiversity loss, the current global distribution of forest CSC is being reshaped (*3*, *10*). Therefore, understanding the underlying factors that influence the global distribution of forest CSC and unraveling the correlations between forest CSC and forest ecosystem productivity and stability have become of great importance for understanding forest carbon dynamics, as well as aiding forest management and conservation.

The global distribution of forest CSC is influenced by a combination of biotic, climatic, and edaphic factors. Biotic factors, such as tree species composition and forest age, can induce changes in the phenotypic characteristics of canopy elements (e.g., leaf size, tree size, and branch architecture) and influence the selection of ecological niches (*11*, *12*), ultimately shaping the space-filling characteristics of canopy elements and consequently altering forest CSC. Climatic factors, such as precipitation and temperature, along with edaphic factors like soil texture and soil nutrient content, can affect forest CSC by shaping regional tree species pools and determining resource accessibility for tree growth (*13*, *14*). Moreover, climatic and edaphic factors can interact with biotic factors through phenotypic plasticity of canopy elements (i.e., the phenotypic characteristics of the same tree species may vary with environmental gradients) (*15*, *16*), leading to variations in forest CSC. Despite the essential role of biotic, climatic, and edaphic factors in modulating forest CSC, our current understanding is primarily limited to regional scales (*17*, *18*), and their relative contributions to forest CSC have not been well quantified at a global scale (*4*).

As for the correlations of forest CSC with forest ecosystem productivity and stability, they remain uncertain on a global scale. Both the effects of forest CSC on forest ecosystem productivity and stability are generally hypothesized to be positive, and this hypothesis is supported by observations in northern hardwood forests, mixed coniferous forests, etc. (*7*, *19*, *20*). Forest stands with higher CSC may exhibit enhanced light interception capabilities through crown complementarity as well as a broader range of strategies to regulate resource allocation (e.g., canopy wind transmission reduction and overshadowing effect), thereby benefiting biomass accumulation and improving resilience to disturbance (*8*, *21*, *22*). However, contradictory observations have also been reported, showing negative or neutral correlations between forest CSC and forest ecosystem productivity and stability (*23*, *24*). It is argued that the asymmetric light competition between overstory and understory trees resulting from high CSC may suppress the understory, leading to lower overall forest ecosystem productivity (*23*, *25*), and the stronger competition in structurally complex forests may reduce the resource availability per individual, potentially increasing sensitivity to disturbances (*24*).

One of the primary challenges hindering current studies is that they are usually conducted at a forest site scale, due to the lack of efficient methods for quantifying forest CSC at a broader spatial scale (*4*, *26*). Recently, advancements in light detection and ranging (lidar) techniques have enabled the accurate quantification of forest CSC (*27*, *28*). In a pioneering effort, Ehbrecht *et al.* (*3*) attempted to map the global distribution of forest CSC by integrating terrestrial lidar data from 294 plots at 20 primary forest sites with climate

[1]State Key Laboratory of Vegetation and Environmental Change, Institute of Botany, Chinese Academy of Sciences, Beijing 100093, China. [2]China National Botanical Garden, Beijing 100093, China. [3]University of Chinese Academy of Sciences, Beijing 100049, China. [4]Institute of Ecology, College of Urban and Environmental Science, Peking University, Beijing 100871, China. [5]School of Biological Sciences and Institute for Climate and Carbon Neutrality, The University of Hong Kong, Pok Fu Lam, Hong Kong, China. [6]Department of Geosciences and Geography, University of Helsinki, Helsinki FI-00014, Finland. [7]Finnish Meteorological Institute, FMI, Helsinki, Finland. [8]Jiangsu Provincial Key Laboratory of Geographic Information Science and Technology, International Institute for Earth System Science, Nanjing University, Nanjing 210023, China. [9]Institute of Remote Sensing and Geographical Information Systems, School of Earth and Space Sciences, Peking University, Beijing 100871, China.
*Corresponding author. Email: ysu@ibcas.ac.cn

variables. The recent advent of the Global Ecosystem Dynamics Investigation (GEDI) spaceborne lidar system offers an alternative approach to explore the global distribution of forest CSC (*29*). With a substantially larger lidar sample size (over 400-million GEDI footprints were used in the current study) and without the uncertainties introduced by auxiliary datasets such as climate variables, GEDI presents an opportunity for more comprehensive analysis. In this study, we present a near-global map of forest CSC using the baseline year 2021. A robust metric, namely, canopy entropy (*30*), was adopted to quantify forest CSC by integrating GEDI data with airborne lidar data from 4000 forest plots (figs. S1 to S3). Through this analysis, we aim to address the following three research questions: (i) How do biotic, climatic, and edaphic factors drive the global distribution of forest CSC? (ii) How does forest CSC relate to forest ecosystem productivity and stability at a global scale? (iii) How do biotic, climatic, and edaphic factors influence the effect of forest CSC on forest ecosystem productivity and stability?

To accomplish this, we compiled a dataset comprising two biotic factors describing species richness and forest age; 10 climatic factors characterizing water resources, temperature, and light conditions; and three edaphic factors detailing soil texture (silt and clay fraction) and soil nutrient contents (table S1). Forest ecosystem productivity was represented by gross primary productivity (GPP) obtained from both the Moderate Resolution Imaging Spectroradiometer (MODIS) product and the Global Orbiting Carbon Observatory-2–based Solar-Induced Chlorophyll Fluorescence (GOSIF) product (table S1), and forest ecosystem stability was assessed from over 20-year MODIS normalized difference vegetation index (NDVI) data using the composite early warning indicator, which quantifies the capacity of ecosystems to withstand perturbations and avoid state shifts (fig. S4) (*31*).

RESULTS AND DISCUSSION

Factors driving the global distribution of forest CSC

Canopy entropy is an efficient metric for quantifying forest CSC, capable of capturing within-canopy structural variations caused by both horizontal and vertical arrangements and occupations of canopy elements (*30*). It is particularly well suited for large-scale applications using multiplatform lidar point clouds with varying point densities, as it exhibits low dependence on point density due to its projected kernel density estimation–based calculation strategy (fig. S5) (*30*). A higher value in canopy entropy indicates a more complex forest canopy structure (Fig. 1A). When compared to independent estimates of canopy entropy derived from airborne lidar data, the forest CSC estimation model based on GEDI data demonstrated a coefficient of determination (R^2) of 0.58 and a normalized root mean square error of 12.35% (Fig. 1B), and a satisfactory estimation accuracy was achieved at the forest biome scale as well (fig. S6). Two primary sources of uncertainty were the relatively low accuracy of canopy cover estimates from GEDI data (fig. S7) and the constrained penetration capability of GEDI in dense forest canopies with multiple vertical layers (e.g., tropical and subtropical moist broadleaf forests; fig. S6).

The generated global map of forest CSC had a spatial resolution of 0.025° × 0.025°, spanning from ~52°S to 52°N (Fig. 1C). The averages of forest CSC and its variability within each pixel across the globe were 10.57 and 0.56, respectively (Fig. 1C and fig. S8). The global map of forest CSC exhibited noticeable spatial heterogeneities (Fig. 1C), with the highest values observed around the equator and 45°S (Fig. 1D). Notably, the spatial distributions and latitudinal patterns remained consistent when aggregating GEDI footprint-level forest CSC estimates into different spatial resolutions (0.005° × 0.005°, 0.01° × 0.01°, and 0.05° × 0.05°) (fig. S9). Among the global forest biomes defined in the Terrestrial Ecoregions of the World (*32*), tropical and subtropical moist broadleaf forests had the highest CSC (mean, 10.65), followed by temperate broadleaf and mixed forests (mean, 10.61), temperate coniferous forests (mean, 10.60), tropical and subtropical coniferous forests (mean, 10.46), temperate savannas (mean, 10.26), tropical and subtropical dry broadleaf forests (mean, 10.18), Mediterranean forests (mean, 10.09), boreal forests (mean, 9.94), tropical and subtropical savannas (mean, 9.89), and flooded savannas (mean, 9.83) (Fig. 1E).

To analyze the factors influencing the global distribution of forest CSC, we chose two factors from each category based on their relative importance in explaining forest CSC through a random forest analysis, given the imbalanced number of biotic, climatic, and edaphic factors (table S1), as well as the strong intercorrelations within each factor category (fig. S10). Among the categories with multiple factors, mean annual temperature (MAT) emerged as the most important temperature-related factor, mean annual precipitation minus potential evapotranspiration (MAP-PET) emerged as the most important water resource–related factor, and soil nitrogen content emerged as the most important soil nutrient–related factor. Consequently, we selected species richness and forest age to represent biotic conditions, MAT and MAP-PET to represent climatic conditions, and soil texture and soil nitrogen content to represent edaphic conditions (Fig. 2A).

On a global scale, MAP-PET emerged as the most influential factor on forest CSC, followed by MAT, forest age, species richness, soil nitrogen content, and soil texture (fig. S11A). Furthermore, MAP-PET consistently ranked among the top three most influential factors in 6 of the 10 forest biomes (fig. S11), in line with findings from previous studies (*3*). However, the dominant factor varied across different forest biomes and generally aligned with the corresponding factor limiting tree growth (fig. S11). In arid and semiarid forest biomes, where water supply is a key limitation for tree growth (*33*), MAP-PET remained the most influential factor (fig. S11, C, H, and J). In temperate and boreal forest biomes, where temperature plays a major role in limiting tree growth (*34*), MAT became the primary driver influencing forest CSC (fig. S11, E to G and I). Tropical and subtropical forests, characterized by short regeneration cycles (*35*), substantial disturbances from human activities in recent decades (*36*), and relatively low soil nutrient content (*37*), were primarily influenced by forest age and soil nitrogen content (fig. S11, B to D). The combined effects of biotic, climatic, and edaphic factors accounted for 77% of the variations in forest CSC across the globe (Fig. 2B). Notably, the combined impact of climatic and edaphic factors on forest CSC outweighed that of biotic factors, and biotic factors contributed to forest CSC mainly through interacting with climatic and edaphic factors (Fig. 2B). This phenomenon held true across forest biomes (fig. S12), highlighting the potential strong phenotypic plasticity of canopy elements in response to variations in environmental conditions (*4*). Even in areas with the same tree species pool, the phenotypic characteristics of canopy elements may vary significantly along environmental gradients, thereby altering forest CSC (*15*).

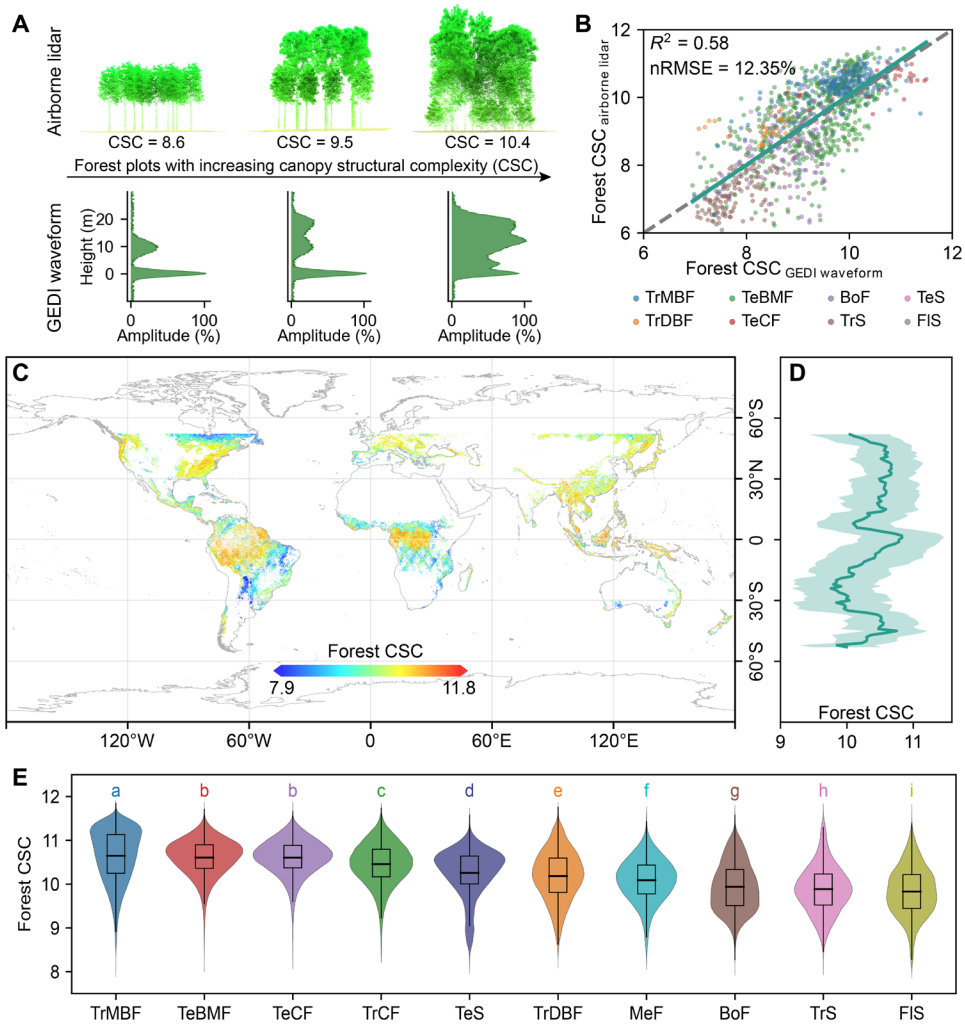

Fig. 1. Global distribution of forest CSC. (**A**) Illustrative examples of airborne lidar data and simulated spaceborne GEDI waveforms for forest stands with varying CSC values. (**B**) Accuracy evaluation of forest CSC estimates derived from simulated GEDI waveforms. The coefficient of determination (R^2) and the normalized root mean square error (nRMSE) are reported. The solid green line represents the fitted line with $P < 0.001$, and the dashed gray line represents the 1:1 line. (**C**) Global forest CSC map estimated from GEDI data at a spatial resolution of 0.025° × 0.025°. (**D**) Latitudinal pattern of forest CSC presented with a 1° interval. The green solid line represents the average forest CSC, and the green shaded area represents one SD. (**E**) Violin and box plots demonstrating the variations in forest CSC within forest biomes defined in the Terrestrial Ecoregions of the World (*32*). The upper, central, and lower horizontal lines in each box correspond to the 25th percentile, mean, and 75th percentile, respectively. The colored letters represent statistical test results (Games-Howell test) among the means, with forest biomes not sharing the same letter considered significantly different ($P < 0.05$). The abbreviations TrMBF, TeBMF, TeCF, TrCF, TeS, TrDBF, MeF, BoF, TrS, and FIS represent tropical and subtropical moist broadleaf forests, temperate broadleaf and mixed forests, temperate coniferous forests, tropical and subtropical coniferous forests, temperate savannas, tropical and subtropical dry broadleaf forests, Mediterranean forests, boreal forests, tropical and subtropical savannas, and flooded savannas, respectively. Further details about the extent of these forest biomes can be found in fig. S1.

Biotic, climatic, and edaphic factors all exerted significant influences on the spatial distribution of forest CSC across the globe (Fig. 2C). The two biotic factors, namely, species richness and forest age, demonstrated significant positive correlations with forest CSC ($P < 0.05$; Fig. 2C). As species richness increases, forest stands gain access to a broader tree species pool, allowing for more efficient ecological niche utilization through complementarity in crown architectures and ultimately leading to higher forest CSC (*4*, *7*). Moreover, older forests have generally experienced long-term successions, fostering the development of more complex forest canopies (*19*). Regarding climatic factors, the water resource–related factor (MAP-PET) also exhibited a positive correlation with forest CSC (Fig. 2C). Regions with abundant water resources can support the growth of tall trees, potentially enhancing forest CSC (*14*). The temperature-related factor (MAT) displayed a hump-shape relationship with forest CSC (Fig. 2C), possibly attributed to the presence of two distinct forest types in tropical regions, i.e., rainforests and savannas (*32*). Both edaphic factors demonstrated positive correlations with forest CSC (Fig. 2C). Higher soil nitrogen content and finer soil texture (i.e., higher silt and clay fraction) can provide better soil conditions, which are advantageous for tree growth, consequently enhancing forest CSC (*38*). It is noteworthy that the correlations between forest CSC and all factors remained unchanged when they were evaluated by partial dependencies derived from random forest regression

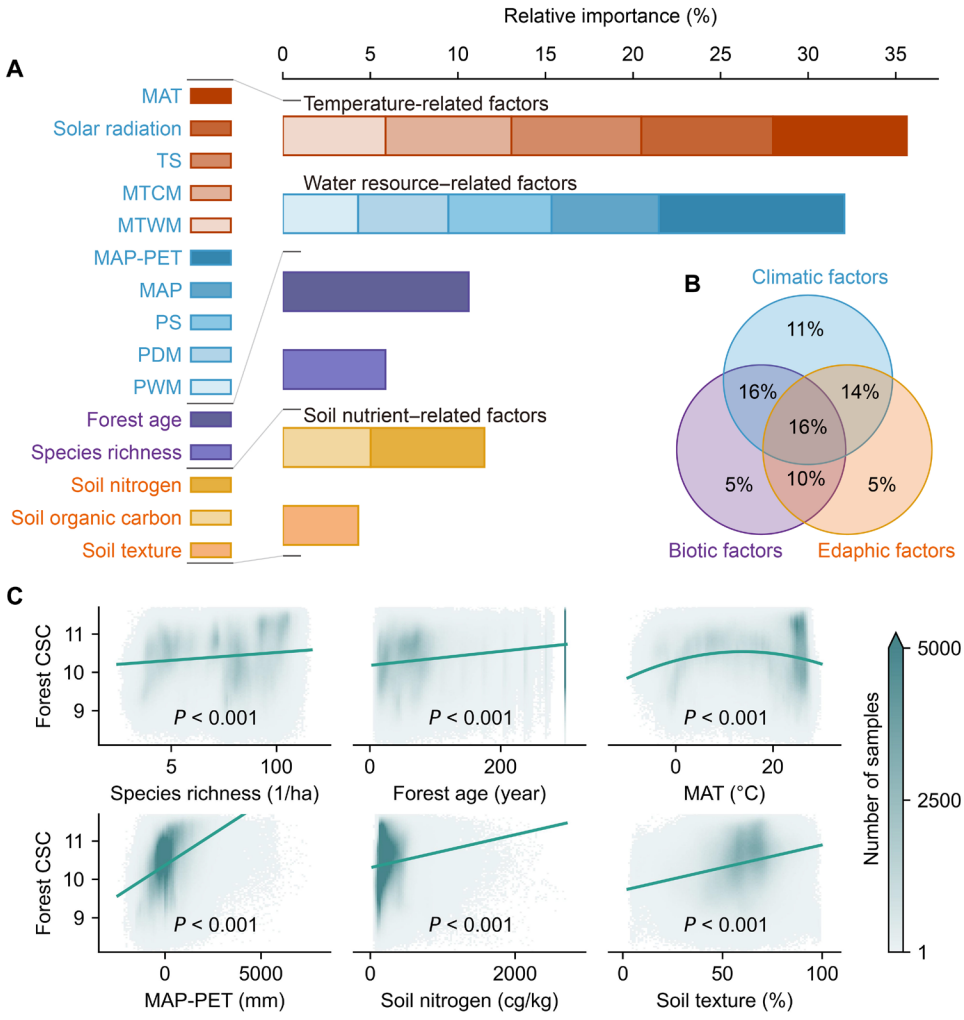

Fig. 2. Factors driving the global distribution of forest CSC. (**A**) Relative importance of biotic, climatic, and edaphic factors in explaining forest CSC. Relative importance was quantified as the increase in node purity through a random forest analysis. MAT, TS, MTCM, MTWM, MAP, PET, PS, PDM, and PWM represent mean annual temperature, temperature seasonality, minimum temperature of the coldest month, maximum temperature of the warmest month, mean annual precipitation, potential evapotranspiration, precipitation seasonality, precipitation of the driest month, and precipitation of the wettest month, respectively. Because of the right-skewed distribution of species richness (fig. S13), it was logarithmically transformed in all subsequent analyses (*61*). (**B**) Collective contributions of biotic, climatic, and edaphic factors to the global distribution of forest CSC. Two factors were selected in each category based on their relative importance in explaining forest CSC. Biotic factors include species richness and forest age, climatic factors include MAT and MAP-PET, and edaphic factors include soil nitrogen content and soil texture (silt and clay fraction). The intersection of circles represents the coupling effect of biotic, climatic, and edaphic factors on forest CSC. (**C**) Relationships between the global distribution of forest CSC and biotic, climatic, and edaphic factors. Forest CSC was evenly grouped into 100 bins based on each factor, and its relationship with each factor was modeled using either weighted linear regression or weighted quadratic regression (if the weighted linear regression result was nonsignificant). The number of data points within each bin was used as the weight in the regressions. The solid green lines represent the fitted lines, and statistical results, including the used regression approach, R^2, and *P*, are reported in table S2.

analyses (fig. S14). Moreover, these relationships within the majority of forest biomes closely mirrored their global counterparts (fig. S15), indicating a potential consistency in the ecological mechanisms governing how biotic, climatic, and edaphic factors influence forest CSC across diverse forest biomes.

Relationships of forest CSC with forest ecosystem productivity and stability

Forest CSC demonstrated positive correlations with forest ecosystem productivity and stability globally and across different forest biomes ($P < 0.05$), with the exception of temperate savannas for productivity (Fig. 3A and tables S3 and S4), suggesting that forest stands with higher CSC exhibited increased productivity and greater resilience to disturbance. These findings provided support for existing hypotheses (*7*, *19*, *22*) and indicated that previous inconsistent observations may be attributed to their limited spatial scales, emphasizing the importance of comprehending the relationships between forest CSC and forest ecosystem productivity and stability from a global perspective. Note that, when evaluating the relationships between forest CSC and forest ecosystem productivity and stability using different forest ecosystem productivity products (i.e., GPP measurements from flux towers and MODIS and GOSIF GPP products), different forest CSC metrics (i.e., canopy entropy, canopy cover, and foliage height diversity), and different spatial resolutions

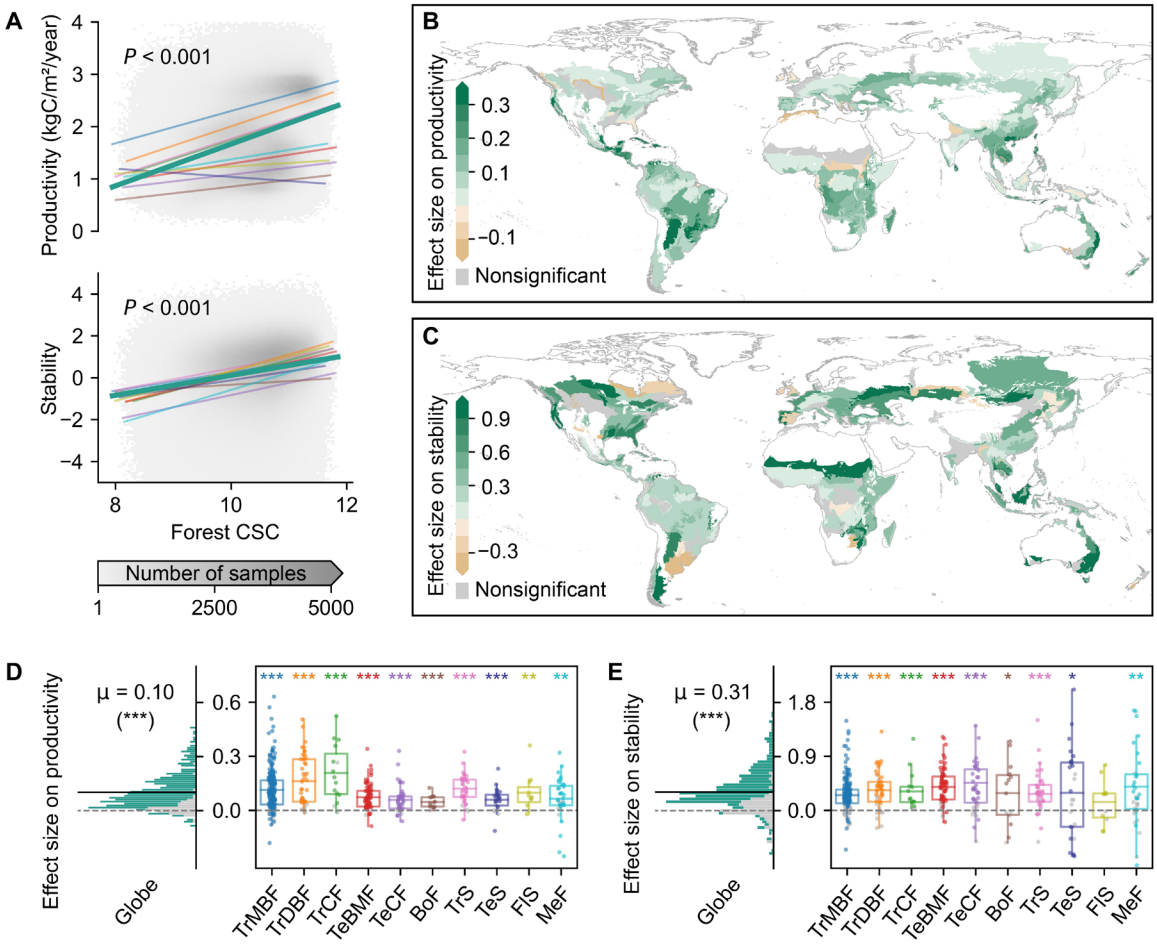

Fig. 3. Forest CSC effects on forest ecosystem productivity and stability. (**A**) Relationships between forest CSC and forest ecosystem productivity and stability on a global scale and within each forest biome. Forest ecosystem productivity was represented by GPP extracted from the MODIS product. The bold solid green lines represent the fitted lines on a global scale, while the non-bolded solid lines represent the fitted lines within each forest biome. The colors of the fitted lines within each forest biome match those in (**D**) and (**E**). Statistical results, including Pearson's correlation coefficient (*r*), slope, and *P*, are reported in tables S3 and S4. (**B**) Distribution of the effect size of forest CSC on forest ecosystem productivity across global forest ecoregions. (**C**) Distribution of the effect size of forest CSC on forest ecosystem stability across global forest ecoregions. Effect sizes were quantified through multilinear regression analyses. (D) Histogram of the effect size of forest CSC on forest ecosystem productivity across global forest ecoregions and its box plot within each forest biome. (E) Histogram of the effect size of forest CSC on forest ecosystem stability across global forest ecoregions and its box plot within each forest biome. The gray bars in the histograms represent forest ecoregions with nonsignificant multilinear regression models or nonsignificant forest CSC effects on forest ecosystem productivity or stability. The solid black lines and μ represent the mean forest CSC effects globally, while the dashed gray line separates forest ecoregions with significant positive effects and significant negative effects. *, **, and *** represent global forests or forest biomes with mean forest CSC effect size significantly greater than 0 at confidence levels of 95%, 99%, and 99.9%, respectively. Abbreviations of forest biomes in the box plots are consistent with those in Fig. 1E.

(i.e., 0.005° × 0.005°, 0.01° × 0.01°, 0.025° × 0.025°, and 0.05° × 0.05), similar results were yielded (Fig. 3A, figs. S16 to S19, and tables S3 and S4). Consequently, only results using canopy entropy as the quantification metric of forest CSC, a spatial resolution of 0.025° × 0.025°, and MODIS GPP product are reported henceforth.

To assess the relationships between forest CSC and forest ecosystem productivity and stability across different forest ecoregions, particularly considering the potential confounding influence of biotic, climatic, and edaphic factors on both forest CSC and forest ecosystem productivity and stability, we further investigated their relationships within each forest ecoregion using multilinear regression. Our analysis covered a total of 496 forest ecoregions identified in the Terrestrial Ecoregions of the World. A multilinear regression model was constructed for forest ecosystem productivity or stability in each forest ecoregion, using forest CSC, species richness, forest age, MAT, MAP-PET, soil nitrogen content, and soil texture as explanatory variables. The coefficients of forest CSC in the regression models served as indicators of the effect sizes of forest CSC.

The multilinear regression models constructed in this study effectively captured the variations of forest ecosystem productivity (mean $R^2 = 0.43$, with $P < 0.05$ in 99.4% of the forest ecoregions) and stability (mean $R^2 = 0.13$, with $P < 0.05$ in 97.0% of the forest ecoregions) (fig. S20). Forest CSC demonstrated a positive effect on forest ecosystem productivity and stability in the majority of forest ecoregions (Fig. 3, B and C). The average effect size of forest CSC on forest ecosystem productivity was 0.10, with 78.0% of the forest

ecoregions showing a significant positive effect ($P < 0.05$), 17.3% showing a nonsignificant effect ($P > 0.05$), and 4.7% showing a significant negative effect ($P < 0.05$) (Fig. 3D). Similarly, the average effect size of forest CSC on forest ecosystem stability was 0.31, with 67.6% of the forest ecoregions showing a significant positive effect ($P < 0.05$), 27.4% showing a nonsignificant effect ($P > 0.05$), and 5.0% showing a significant negative effect ($P < 0.05$) (Fig. 3E). The average effect sizes of forest CSC on forest ecosystem productivity and stability were positive in all forest biomes and significantly different from 0 ($P < 0.05$), except for the average effect size of forest CSC on forest ecosystem stability in flooded savannas (Fig. 3, D and E).

While forest CSC generally had a positive effect on forest ecosystem productivity and stability, the effect size varied substantially across forest ecoregions (the SD of effect size was 0.11 for productivity and 0.42 for stability) (Fig. 3, B and C), and the patterns of their spatial variations generally aligned with those derived from different forest ecosystem productivity products, different forest CSC metrics, and different spatial resolutions (Fig. 3, B and C, and figs. S17 to S19 and S21). It should be noted that the predominantly positive effects of forest CSC on forest ecosystem productivity and stability were also observed using linear regression with forest CSC as the sole explanatory variable (fig. S22). However, the effect sizes from linear regression models were generally larger than those from multilinear regression models (fig. S22), indicating that linear regression results might include the confounding effects of biotic, climatic, and edaphic factors on both forest CSC and forest ecosystem productivity and stability.

Factors influencing the effect size of forest CSC on forest ecosystem productivity and stability

The spatial heterogeneity in the size of forest CSC effects on forest ecosystem productivity and stability was found to be influenced by variations in biotic, climatic, and edaphic factors among forest ecoregions. Specifically, the effect size of forest CSC on forest ecosystem productivity exhibited positive correlations with species richness, MAT, and soil texture (Fig. 4, A, C and F). Forests characterized by high species richness may offer increased opportunities for the inclusion of shade-tolerant tree species, fostering the formation of functionally diverse tree species communities in line with the physiological tolerance hypothesis (*39*). This, in turn, may enable more efficient utilization of ecological niches beneath the tallest trees. Consequently, a similar magnitude of CSC increase in forests with high species richness may have a stronger positive effect on light and water interception capacity through crown complementarity (*6*, *40*, *41*), amplifying the overall positive impact of forest CSC on forest ecosystem productivity. Notably, the phenomenon of overyielding associated with species richness has been observed in planted forests (*7*, *42*), and our findings underscore its potential existence in natural forests as well. The positive correlation of MAT and soil texture may be attributed to site conditions characterized by abundant light resources and improved soil fertility and water retention capacity (*6*, *38*). These conditions that can support the growth of trees using different aboveground and belowground ecological niches, consequently enhancing the positive effect of forest CSC on forest ecosystem productivity through complementarity.

In contrast, forest age exhibited a negative correlation with the effect size of forest CSC on forest ecosystem productivity (Fig. 4B), aligning with the findings from site-level studies (*43*). This may be associated with the forest regeneration process, whereby fast-growing species gradually give way to slower-growing species (*44*), thereby weakening the positive effect of forest CSC. In our study, 12 of the 23 forest ecoregions with negative correlations between forest CSC and forest ecosystem productivity have a forest age exceeding 100 years. Despite that the correlation between MAP-PET and the effect size of forest CSC on forest ecosystem productivity was nonsignificant, it displayed a weak negative trend ($P = 0.060$; Fig. 4D). This is potentially caused by the increasing tree height in areas with abundant water resources (*14*, *45*). Although increasing tree height can enhance forest CSC and the productivity of overstory trees, it can also suppress the growth of understory trees due to the intensified selection effect (*23*). Consequently, this phenomenon may diminish the overall positive effect of forest CSC on forest ecosystem productivity (*25*).

Regarding the effect size of forest CSC on forest ecosystem stability, all biotic, climatic, and edaphic factors, except for forest age and soil nitrogen content, exhibited significant negative correlations with it (Fig. 4, G to L). The negative correlation of species richness might be attributed to the insurance effect. As species richness increases, its capacity to ensure forest ecosystem stability strengthens (*46*), potentially reducing the significance of the effect of forest CSC on forest ecosystem stability. It is worth noting that species richness and forest CSC have been observed to exhibit a coupled influence on forest ecosystem stability (*47*); however, the precise mechanism underlying this coupling relationship needs further investigation. The negative correlations observed in MAT, MAP-PET, and soil texture could be associated with resource availability in different forest ecoregions. Forests in areas with high MAT, MAP-PET, and soil texture typically occupy abundant light and water resources, rendering the regulation of forest CSC on light and water potentially less important for maintaining forest ecosystem stability. Conversely, in areas characterized by harsh environmental conditions with limited light or water resources, the regulation of forest CSC on light and water may become a crucial process in responding to disturbances triggered by extreme weather events (*48*). These findings emphasize the importance of considering the effect of forest CSC on forest ecosystem stability in forest management practices within such regions.

The relationships of the effect sizes of forest CSC on forest ecosystem productivity and stability with biotic, climatic, and edaphic factors persisted when assessed through partial dependencies derived from random forest regression analyses (fig. S23), and the effect size of forest CSC on forest ecosystem productivity was found to be independent of the effect size of forest CSC on forest ecosystem stability (fig. S24), despite both demonstrating positive values in most forest ecoregions. Furthermore, the relationships of the effect sizes of forest CSC on forest ecosystem productivity and stability with biotic, climatic, and edaphic factors remained consistent when assessed at various spatial scales (i.e., $0.005° \times 0.005°$, $0.01° \times 0.01°$, $0.025° \times 0.025°$, and $0.05° \times 0.05$) (tables S5 and S6), suggesting that the ecological principles governing how forest CSC influences forest ecosystem productivity and stability may be consistent across spatial scales. However, note that all spatial scales used in this study were relatively coarse due to the limitation in the spatial resolution of the available datasets (table S1), and, thus, the impact of spatial scale on the effect sizes of forest CSC on forest ecosystem productivity and stability needs to be further investigated at a finer spatial scale by incorporating field measurements and near-surface lidar data from ecological observation networks.

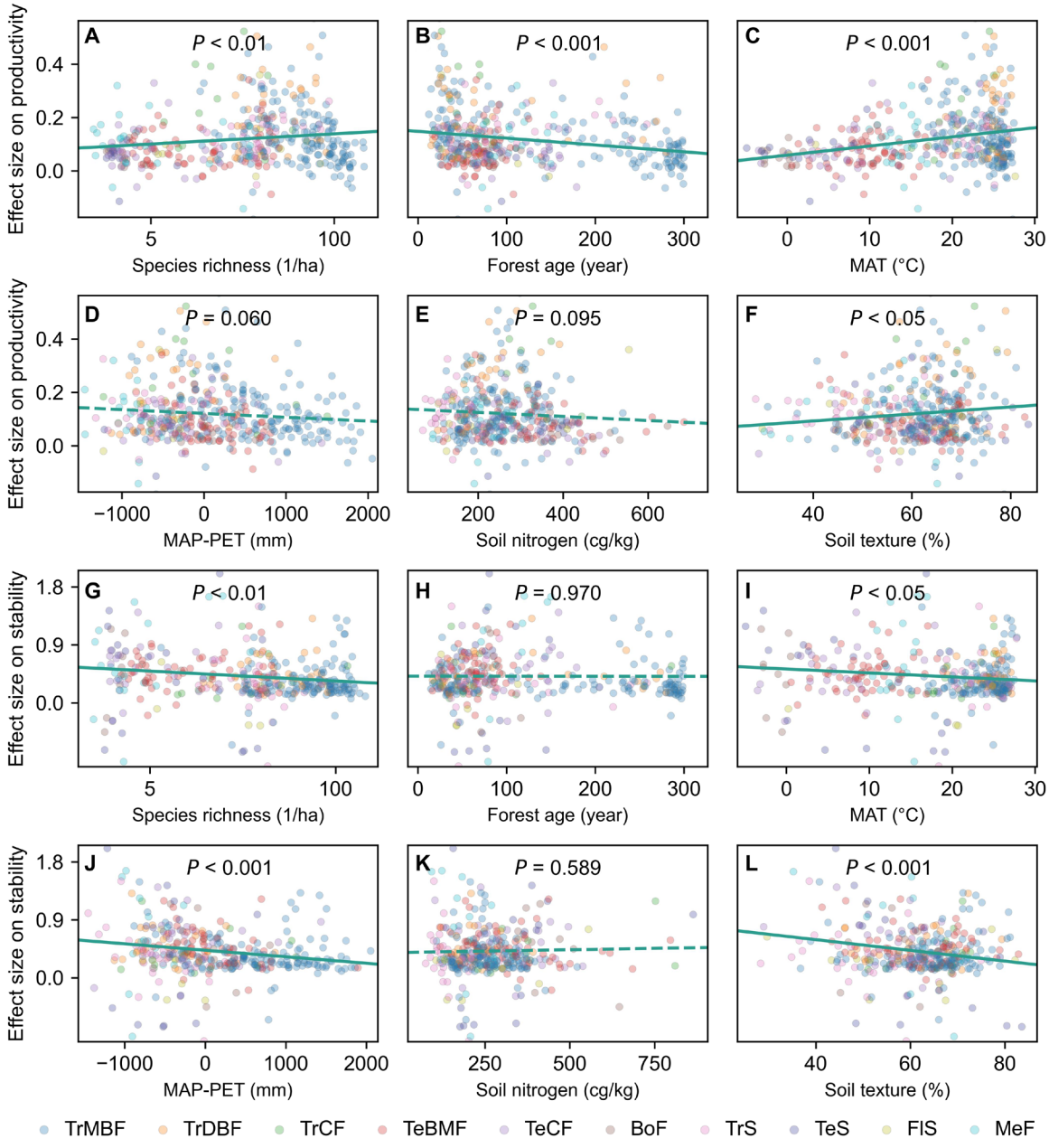

Fig. 4. Relationships of the effect sizes of forest CSC on forest ecosystem productivity and stability with biotic, climatic, and edaphic factors. (**A** to **F**) Relationships between the effect size of forest CSC on forest ecosystem productivity and species richness, forest age, MAT, MAP-PET, soil nitrogen content, and soil texture. (**G** to **L**) Relationships between the effect size of forest CSC on forest ecosystem stability and species richness, forest age, MAT, MAP-PET, soil nitrogen content, and soil texture. The solid green lines represent significant fitted lines with $P < 0.05$, while the dashed green lines represent nonsignificant fitted lines with $P > 0.05$. Notably, only forest ecoregions with a significant effect on forest ecosystem productivity or stability were included here.

Implications for forest management and conservation

Considering the predominantly positive relationships between forest CSC and forest ecosystem productivity and stability, we emphasize the urgent need to integrate forest CSC into the development of sustainable forest management and conservation plans. Now, the CSC of managed forests is significantly lower than that of intact forests within the same ecoregions ($P < 0.001$) (Fig. 5A), highlighting the substantial potential for improving CSC in managed forests. The differences in CSC between intact and managed forests are positively linked to their disparities in forest ecosystem productivity and stability ($P < 0.05$) (Fig. 5B), suggesting that the neglect of forest CSC in forest management may contribute to the relatively lower ecosystem productivity and stability observed in managed forests. Given the observed fact that the enhancing effects of forest CSC on forest ecosystem productivity and stability in managed forests are significantly stronger than those in intact forests (Fig. 5C), we

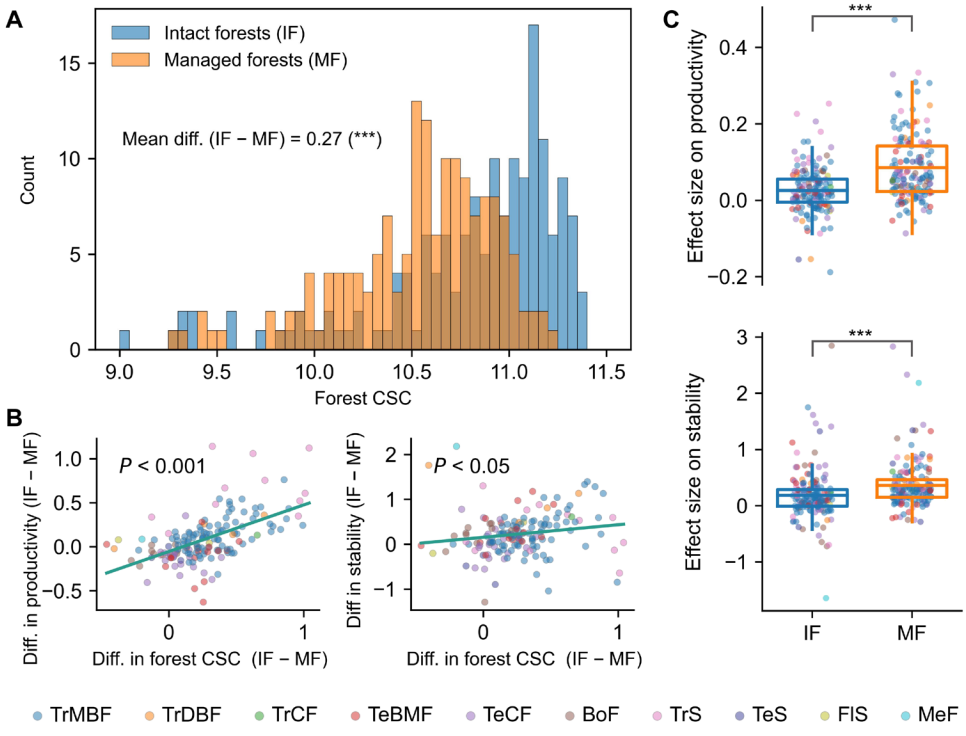

Fig. 5. Differences in forest CSC and its impact on ecosystem productivity and stability in intact and managed forests. (**A**) Histograms of forest CSC within ecoregions containing both intact and managed forests. Only forest ecoregions with over 70 pixels (0.025° × 0.025°) of both intact forests and managed forests are included here (fig. S25). (**B**) Correlations of differences in forest CSC between intact and managed forests with differences in ecosystem productivity and stability. The solid green lines represent the fitted lines. (**C**) Box plots of the effect sizes of forest CSC on ecosystem productivity and stability in intact and managed forests. *** represents significant differences at a confidence level 99.9%, and "diff." is an abbreviation for "difference."

recommend giving particular attention to forest CSC and its accompanying structural attributes (such as canopy height and leaf area index) (*4*, *27*) in managed forests. This focus will enable us to fully harness their ecosystem functions in carbon sequestration and the maintenance of forest ecosystem stability.

Regarding intact forests, our comprehensive map, which accurately delineates the global distribution of forest CSC, along with our findings on the factors influencing the effect sizes of forest CSC on forest ecosystem productivity and stability, can serve as a valuable benchmark for understanding their responses to climate change, identifying forest ecoregions at high risk, and formulating appropriate conservation plans. However, it is crucial to acknowledge that climate change is reshaping the global distribution of forest CSC (*3*, *9*), and there remains a substantial knowledge gap regarding the temporal dynamics of forest CSC in response to these global climate changes (*4*). The primary challenge lies in the limited availability of time-series spaceborne lidar data necessary to assess the temporal variations in forest CSC. Recent studies have suggested that synthetic aperture radar might be responsive to forest CSC changes (*49*). The integration of lidar and radar data holds promise for monitoring the temporal dynamics of forest CSC. Moreover, it is noteworthy that current dynamic global vegetation models often overlook the interactions among climate change, forest CSC, and forest ecosystem productivity and stability (*50*). Further investigations are needed to explore how to effectively incorporate the influence of forest CSC on forest ecosystem productivity and stability and its potential feedback to climate.

MATERIALS AND METHODS

Airborne lidar data

To map the global distribution of forest CSC, this study used two types of lidar data: airborne lidar data and spaceborne lidar data. Airborne lidar offers precise three-dimensional location information of canopy elements through dense point clouds (examples shown in Fig. 1A) and is considered an ideal data source for quantifying forest CSC (*27*, *30*). Here, we collected airborne lidar data (including both aircraft-based and drone-based measurements) from 4000 forest plots covering eight distinct forest biomes defined in the Terrestrial Ecoregions of the World, including tropical and subtropical moist broadleaf forests (1157 plots), tropical and subtropical dry broadleaf forests (100 plots), temperate broadleaf and mixed forests (1536 plots), temperate coniferous forests (100 plots), boreal forests (500 plots), tropical and subtropical savannas (555 plots), temperate savannas (26 plots), and flooded savannas (26 plots) (fig. S1 and table S7). These lidar data were acquired either through self-collection efforts (mainly in China) or downloaded from publicly accessible data centers, such as the Goddard's LiDAR, Hyperspectral and Thermal imager data center and the Oak Ridge National Laboratory Distributed Active Archive Center (table S7). All lidar data were acquired between 2009 and 2022, and each plot had a size of 25 m by 25 m, matching the size of GEDI footprints. In addition to these 4000 forest plots, we collected airborne lidar data from an additional 375 forest plots located in 20 National Ecological Observatory Network (NEON) forest sites (table S7 and fig. S16), serving the purpose of validating the relationship between forest CSC and forest

ecosystem productivity. All these plots were established in association with the flux towers within these sites, each covering an area of 40 m by 40 m (*51*). The airborne lidar data for these plots were acquired after the year 2019.

All collected airborne lidar data were preprocessed following the same streamline procedure, including outlier removal, filtering, and normalization. Outlier removal aimed to mitigate the influence of noise points caused by high-flying objects (e.g., birds and powerlines) and the multipath effect, which were identified by determining whether the distance between a point and its neighboring points exceeding a threshold of avg. + 2 × std. (where avg. and std. are the average and SD of point distance) (*30*). Filtering was performed to classify lidar points into ground and nonground points, and an improved progressive triangulated irregular network densification filtering algorithm was used in this study (*52*). Normalization was conducted to minimize the impact of terrain elevations on lidar points, which was achieved by subtracting the elevations of lidar points by their corresponding ground elevations (*30*). The aforementioned preprocessing steps were implemented using the LiDAR360 software (GreenValley International, Beijing, China).

Spaceborne lidar data

Although airborne lidar demonstrates robust capabilities in quantifying forest CSC, its global-scale application is hindered by limited spatial coverage (*28*). Spaceborne lidar presents a promising opportunity to overcome this limitation and achieve the goal of mapping the global distribution of forest CSC (*29*). In this study, we used GEDI, a spaceborne lidar system specifically designed for acquiring three-dimensional vegetation structural information launched in December 2018 (*29*). It provides coverage of the Earth's surface from ~52°N to 52°S and consists of three lasers that are split and beam-dithered, generating eight parallel ground tracks with an interval of ~600 m. Each laser emits laser beams at a wavelength of 1064 nm with a frequency of 242 Hz, illuminating footprints with an approximate diameter of 25 m, spaced 60 m apart from each other along the track. Each footprint records the returned laser energy as a function of time at a 1-ns interval, resulting in waveform data (examples shown in Fig. 1A). In this study, we downloaded all GEDI L2B data (version 2) between April 2019 and December 2021 from the Land Processes Distributed Active Archive Center operated by the US Geological Survey (https://lpdaac.usgs.gov).

To ensure data quality, all collected GEDI footprints underwent filtering based on three criteria. First, the footprints were required to be located within forested areas, determined by evaluating whether the canopy height exceeded 5 m and the canopy cover was above 10%, following the forest definition provided by the Food and Agriculture Organization (*53*). The canopy height and canopy cover values were extracted from the GEDI L2B product, recorded in the respective fields of "rh100" and "cover." Second, the footprints should be collected during the leaf-on season, as determined by the phenology attribute recorded in the field of "leaf_on_cycle" of the GEDI L2B product. Last, the footprints needed to have a quality flag of 1 recorded in the field of "l2b_quality_flag" of the GEDI L2B product, indicating good data quality by considering factors such as waveform shot energy, sensitivity, and amplitude (*29*). Ultimately, a total of 409,537,792 GEDI footprints met these filtering criteria and were retained for mapping the global distribution of forest CSC (fig. S2).

Forest ecosystem productivity and stability data

This study focused on two key forest ecosystem functions associated with carbon dynamics: forest ecosystem productivity and stability. To ensure the reliability of the findings, forest ecosystem productivity was assessed using two independent forest GPP products, namely, the MODIS MOD17A3HGF GPP product (version 6.1) and the GOSIF GPP product (table S1). The MODIS MOD17A3HGF GPP product is a widely recognized and extensively used global GPP dataset (*54*). It provides annual GPP information at a spatial resolution of 500 m by 500 m and is derived by aggregating 8-day MODIS GPP estimates within a year, which are calculated using the light use efficiency concept (*54*). The GOSIF GPP product is developed by establishing linear regression models between ground-based GPP measurements and solar-induced fluorescence measurements obtained from the Orbiting Carbon Observatory-2, and has a spatial resolution of 0.05° × 0.05° (*55*).

In addition to the two satellite-based GPP products, we collected in situ GPP measurements from 20 flux towers in the NEON study sites and 79 flux towers from the AMERIFLUX dataset (https://ameriflux.lbl.gov) (table S1). These data were used to validate the relationship between forest CSC and forest ecosystem productivity observed from the satellite-based GPP products. Corresponding to the airborne lidar data from the 20 NEON study sites (fig. S16), we averaged the available GPP measurements from 2017 to 2021 at each NEON site to represent its forest ecosystem productivity, mitigating the impact of climate conditions on single-year GPP measurements. The GPP measurements from the 79 flux towers were matched with GEDI-derived forest CSC estimates using the following criteria: (i) coverage by our GEDI-derived forest CSC estimates and (ii) at least 1 year of GPP measurements after 2015. We retained 35 of the 79 flux towers (fig. S16), and the multiyear average GPP measurements after the year 2015 were used to represent forest ecosystem productivity at these sites.

Forest ecosystem stability, defined as the capacity of ecosystems to withstand perturbations and avoid state shifts, was evaluated using the composite early warning indicator derived from time-series NDVI. This composite indicator, developed on the basis of the theory of "critical slowing down" and the fold catastrophe model, has gained widespread usage in large-scale ecosystem stability evaluations (*31*, *56*, *57*). Typically, it consists of four components, including autocorrelations at first lag (which measures the similarity between consecutive NDVI observations), SD (which quantifies the variability of times-series NDVI observations), the magnitude of skewness (which assesses the asymmetry of times-series NDVI observations), and kurtosis (which evaluates the degree of "tailedness" of time-series NDVI observations). The composite early warning indicator is computed as the sum of the four components after being normalized (*57*).

In this study, we used the MODIS MOD13A2 NDVI product spanning from 2000 to 2021 to calculate the composite early warning indicator (table S1 and fig. S4). The MODIS MOD13A2 product offers global NDVI observations at a spatial resolution of 1 km by 1 km and a temporal resolution of 16 days (*58*). To mitigate the impact of cloud contamination and account for the influence seasonal vegetation dynamics, we used the maximum-value composite approach to generate a 22-year annual maximum NDVI composite dataset (*59*). In addition, we detrended the time-series NDVI data using a linear model to satisfy the stationary hypothesis and enhance the sensitivity of the composite early

warning indicator (*57*). Note that a higher value in the composite early warning indicator signifies a less stable forest ecosystem. To improve clarity, we applied a multiplication factor of −1 to the final value, thereby reversing the interpretation of the composite early warning indicator as a higher value signifying a more stable forest ecosystem.

Biotic, climatic, and edaphic factors

To investigate how different biotic, climatic, and edaphic factors influence the global distribution of forest CSC and its effects on forest ecosystem productivity and stability, we compiled a dataset comprising two biotic factors, 10 climatic factors, and three edaphic factors (table S1). The two biotic factors included species richness and forest age. Species richness was extracted from a global map of local tree species richness at a spatial resolution of 0.025° × 0.025°, which was generated on the basis of a forest inventory database with individual tree information and local biophysical characteristics (*60*). To account for the right-skewed distribution of global species richness (fig. S13), a logarithm transformation was applied in our analyses (*61*). Forest age information was obtained from a global forest age product with a spatial resolution of 1 km by 1 km, which was mapped using a machine learning method trained on forest inventories, biomass data, and climate data (*62*).

The 10 climatic factors primarily pertain to temperature and water resources conditions (table S1). The factors related to temperature conditions encompassed MAT, solar radiation, maximum temperature of the warmest month, minimum temperature of the coldest month, and temperature seasonality. The factors related to water resources consisted of MAP, MAP-PET, precipitation of the wettest month, precipitation of the driest month, and precipitation seasonality. All climatic factors, except for PET, were derived from the WorldClim (version 2.1) at a spatial resolution of 1 km by 1 km (*63*). PET data were obtained from the global aridity index and PET database (version 3), which used the Penman-Monteith reference evapotranspiration equation for calculation (*64*).

The three edaphic factors primarily pertain to nutrients and soil texture (table S1). The factors related to nutrients included soil nitrogen content and soil organic carbon content. Soil texture was represented by the sum of silt and clay fractions. All edaphic factors were derived from topsoil properties provided by SoilGrids (version 2.0) in three standard layers (i.e., depth intervals of 0 to 5 cm, 5 to 15 cm, and 15 to 30 cm) at a spatial resolution of 250 m by 250 m (*37*). For each factor, we calculated the mean from its values in the three layers using the depth and bulk density of each layer as the weights.

Mapping global forest CSC through the integration of airborne and spaceborne lidar data

Various indices, such as canopy cover, foliage height diversity, canopy top rugosity, and fractal dimension, have been used to quantify forest CSC (*27*). However, these indices may fail to capture variations in forest CSC caused by horizontal or vertical arrangements and occupations of canopy elements (*26*, *30*). Canopy entropy, a robust forest CSC quantification index using a classical measure of complexity, entropy, is directly calculated from original lidar point clouds and fully considers the space occupation characteristics of all canopy elements (*30*). It demonstrates robust performance in quantifying forest CSC and integrates a Mann-Kendall test–based resampling strategy and a projected kernel density estimation–based strategy to reduce dependence on point density, making it well suited for large-scale applications using lidar point clouds from different platforms with varying point densities (*30*). Therefore, canopy entropy was selected as the index to quantify forest CSC in this study.

Canopy entropy consists of three components, including the projected canopy entropy of the *XY* plane (CE_{XY}), the projected canopy entropy of the XZ plane (CE_{XZ}), and the projected canopy entropy of the *YZ* plane (CE_{YZ}), where *X*, *Y*, and *Z* represent south, east, and the zenith direction, respectively, and the final canopy entropy estimate is calculated as follows

$$CE = \sqrt{CE_{XY}^2 + CE_{XZ}^2 + CE_{YZ}^2} \quad (1)$$

where CE represents canopy entropy. Unfortunately, canopy entropy can only be calculated from small-footprint lidar data in the form of point clouds (*30*). As previously mentioned, GEDI provides large-footprint waveform observations, which cannot be directly used for calculating canopy entropy. To address this, we developed a method that combines airborne lidar data with GEDI data to map the global distribution of forest CSC (fig. S3). In this method, two forest CSC–related metrics, namely, foliage height diversity and canopy cover, were extracted from the GEDI L2B product (recorded in the fields of "fhd_normal" and "cover") to estimate the three components of canopy entropy. Our previous studies have found that foliage height diversity is closely related to the two vertical components of canopy entropy (CE_{XZ} and CE_{YZ}), while canopy cover is strongly associated with the horizontal component (CE_{XY}) (*30*). Leveraging these findings, we constructed two linear regression models to estimate the canopy entropy components

$$CE_{XY} = a_1 \times CC + b_1 \quad (2)$$

$$\sqrt{CE_{XZ}^2 + CE_{YZ}^2} = a_2 \times FHD + b_2 \quad (3)$$

where CC represents canopy cover; FHD represents foliage height diversity; and a_1, b_1, a_2, and b_2 denote the four regression coefficients and constants.

To solve the above two linear regression models, we used airborne lidar–derived canopy entropy as the reference data. Specifically, canopy entropy values were calculated for all 4000 forest plots, and a random subset of 70% of these plots was selected as training samples. It is important to mention that, during the calculation process, all ground points from the airborne lidar data were omitted (*30*). To overcome the challenge posed by the spatial mismatch between GEDI and airborne lidar data, primarily caused by the geolocation error of GEDI footprints (~10 m) (*65*), as well as the temporal mismatch in their data acquisition years (table S7), we used the GEDI simulator provided in the R package rGEDI to generate simulated GEDI waveforms from airborne lidar data (fig. S3), which has demonstrated its accuracy across various forest types (*66*). Using the GEDI simulator presents a dependable approach for incorporating spatially and temporally mismatched airborne lidar data into the development of estimation algorithms for forest structural attributes from GEDI waveforms, as successfully implemented in previous studies (*67*). With the simulated GEDI waveforms, foliage

height diversity and canopy cover were calculated using the GEDI simulator as well, which were then paired with airborne lidar–derived canopy entropy components to solve the regression models.

Our findings further confirmed significant correlations of canopy cover and foliage height diversity with the canopy entropy components, but the correlation for canopy cover ($r = 0.58$) was notably weaker than that for foliage height diversity ($r = 0.81$) (fig. S7, A and B). This weaker correlation may be attributed to the relatively higher uncertainty associated with GEDI-derived canopy cover estimates (fig. S7, C to F). Nevertheless, when evaluating the results using the remaining independent 30% forest plots with airborne lidar data, the estimated canopy entropy still demonstrated satisfactory accuracy (Fig. 1B). Therefore, we applied the two derived regression models to all GEDI footprints and calculated the canopy entropy of global forests at the footprint level. The footprint-level canopy entropy estimates were then aggregated into 0.025° × 0.025° pixels, and the value of each pixel was calculated as the average canopy entropy of all footprints within it. The resulting canopy entropy map was used to quantify the global distribution of forest CSC in this study. Furthermore, to evaluate the impact of spatial scale, we generated three additional global forest CSC maps with spatial resolutions of 0.005° × 0.005°, 0.01° × 0.01°, and 0.05° × 0.05°, using the same aggregation approach.

Statistical analyses

To examine the spatial variations in the global distribution of forest CSC, we analyzed its latitudinal pattern using a 1° interval and summarized its statistics within each forest biome through violin and box plots. The differences in means of forest CSC among forest biomes were assessed using the Games-Howell test, a nonparametric test that does not assume equal variances and sample sizes (*68*). Given the strong intercorrelations within biotic, climatic, and edaphic factors (fig. S10) and their imbalanced numbers (table S1), we chose two factors from each category to analyze their influence on the global distribution of forest CSC. The selection process involved assessing the relative importance of each factor in contributing to forest CSC through a random forest analysis. Random forest is a nonparametric machine learning approach that constructs an ensemble of decision trees to prevent overfitting (*69*). Here, we built a random forest model with forest CSC as the dependent variable and all 15 biotic, climatic, and edaphic factors as explanatory variables. The relative importance of each factor was measured by the increase in node purity. To further distinguish the unique characteristics of different climatic factors, we further categorized them into two subcategories: temperature-related factors (including MAT, solar radiation, maximum temperature of the warmest month, minimum temperature of the coldest month, and temperature seasonality) and water resource–related factors (including MAP, MAP-PET, precipitation of the wettest month, precipitation of the driest month, and precipitation seasonality). Similarly, edaphic factors were also divided into two subcategories: soil texture– and soil nutrient–related factors (soil nitrogen content and soil organic carbon content). Eventually, for subcategories with multiple factors, we selected the factor with the largest contribution to forest CSC and used it in the subsequent analyses.

The relative importance of the selected biotic, climatic, and edaphic factors in driving forest CSC on a global scale and within each forest biome was assessed using random forest analyses as well, with the increase in node purity used as the measure of relative importance (fig. S11). The variance partitioning method was used to assess the individual and combined contributions of biotic, climatic, and edaphic factors on forest CSC (*60*). Specifically, we constructed seven separate random forest models using different combinations of biotic, climatic, and edaphic factors as explanatory variables and quantified the variance explanation of each model using R^2, denoted as a for the model with only biotic factors, b for the model with only climatic factors, c for the model with only edaphic factors, d for the model with biotic and climatic factors, e for the model with biotic and soil factors, f for the model with climatic and soil factors, and g for the model with all factors (*60*). The independent contribution of biotic factors; the independent contribution of climatic factors; the independent contribution of edaphic factors; the combined contribution of biotic and climatic factors; the combined contribution of biotic and edaphic factors; the combined contribution of climatic and edaphic factors; and the combined contribution of biotic, climatic, and edaphic factors were then calculated as $g - f$, $g - e$, $g - d$, $a + b - d$, $a + c - e$, $b + c - f$, and $a + b + c + g - d - e - f$, respectively. It should be noted that the variance partitioning analysis was also performed within each forest biome to evaluate the consistency of the results across different forest biomes.

To investigate the nature of the influence of biotic, climatic, and edaphic factors on forest CSC, their correlations with forest CSC were examined both globally and within each forest biome. Given the extensive number of forest CSC observations from our generated global map (over 3.7 million data points) and the nonuniform distribution of certain factors (e.g., MAP-PET) (fig. S13), we used weighted linear regression or weighted quadratic regression to assess the correlation between forest CSC and each factor (*70*). Weighted quadratic regression was used only when the weighted linear regression result was nonsignificant. To achieve this, forest CSC was evenly grouped into 100 bins along each factor, and the number of observations within each bin was used as the weight. Furthermore, we used partial dependence values derived from the random forest method to further assess their correlations, which enabled us to isolate the influence of each factor and evaluate its individual impact on forest CSC, while accounting for the influences of other factors (*71*).

To investigate the relationships between forest CSC and forest ecosystem productivity and stability, we used the linear regression method both on a global scale and within each forest biomes. Given the potential confounding effect of biotic, climatic, and edaphic factors on both forest CSC and forest ecosystem productivity and stability, we further used multilinear regression to quantify the effect size of forest CSC on forest ecosystem productivity or stability within each forest ecoregion sharing a similar biological and environmental history

$$F = \alpha \cdot \mathrm{CSC} + \sum_{i}^{n} \beta_i \cdot \mathrm{Factor}_i \quad (4)$$

where F represents forest ecosystem productivity or stability; Factor_i represents the biotic, climatic, and edaphic factors (including species richness, forest age, MAT, MAP-PET, soil nitrogen content, and soil texture); and the coefficient α was defined as the effect size of forest CSC on forest ecosystem productivity or stability. The delineation of forest ecoregions was determined using the Terrestrial Ecoregions of the World (*32*, *46*). Forest ecoregions with fewer than 70 observations (10 times the number of explanatory variables in the multilinear regression) were excluded from the multilinear regression analysis (*46*). A total of 496 forest ecoregions were eventually

included in the analysis. Note that the data used in the multilinear regression models were not standardized to ensure comparability of effect sizes across forest ecoregions. The effect sizes across these forest ecoregions were summarized on a global scale using histograms and within each forest biomes using boxplots, and whether their means were significantly greater than zero was tested using the one-sided *t* test. The R^2 values of the multilinear regression models and the significance levels of the effect sizes were also reported.

To assess the robustness of the observed relationships between forest CSC and forest ecosystem productivity and stability, we repeated the abovementioned linear regression and multiple linear regression analyses using different satellite GPP products (MODIS MOD17A3HGF GPP product and GOSIF GPP product), forest CSC metrics (canopy entropy, canopy cover, and foliage height diversity), and spatial resolutions (0.005° × 0.005°, 0.01° × 0.01°, 0.025° × 0.025°, and 0.05° × 0.05). Canopy cover and foliage diversity were directly aggregated from the records (cover and fhd_normal) in the GEDI L2B product. Given the varying spatial resolutions of the compiled dataset of forest ecosystem productivity and stability, as well as biotic, climatic, and edaphic factors, we unified the spatial resolutions into a targeted spatial resolution. The average resampling method was used for data with a spatial resolution higher than the targeted spatial resolution, and the resampling method based on bilinear interpolation was used for data with a spatial resolution lower than the targeted spatial resolution. In addition, we assessed the relationship between forest CSC and forest ecosystem productivity through linear regression using in situ GPP measurements from flux towers. For in situ GPP measurements from the 20 NEON study sites, they were compared with their corresponding airborne lidar–derived canopy entropy estimates, while, for in situ GPP measurements from the retained 35 flux towers in AMERIFLUX, they were compared with GEDI-derived canopy entropy estimates.

To better understand the spatial heterogeneities in the effect sizes of forest CSC on forest ecosystem productivity and stability, we conducted analyses to examine their relationships with biotic, climatic, and edaphic factors using linear regression. The biotic, climatic, and edaphic factors for each ecoregion were calculated as their average values within that specific ecoregion. To assess the robustness of the observed relationships, we further evaluated them across various spatial scales (0.005° × 0.005°, 0.01° × 0.01°, 0.025° × 0.025°, and 0.05° × 0.05) and using partial dependence values derived from the random forest method.

To characterize the differences in forest CSC and their effects on ecosystem productivity and stability in intact and managed forests, we further filtered forest ecoregions containing both intact and managed forests. The extent of intact forests was obtained from the intact forest landscapes data (*72*), while forests not covered by intact forests were considered as managed forests (*31*). Only forest ecoregions with more than 70 pixels (0.025° × 0.025°) of both intact and managed forests were retained, resulting in a total of 159 forest ecoregions included in the analysis (fig. S25). To assess whether there was a significant difference between the means of forest CSC in intact and managed forests, the two-sided paired *t* test was used. Moreover, we examined the relationships of differences in mean forest CSC between intact and managed forests of each forest ecoregion with differences in mean forest ecosystem productivity and stability using linear regressions. Last, we calculated the effect sizes of forest CSC on forest ecosystem productivity and stability for intact forests and managed forests, separately, in each forest ecoregion. The differences in effect sizes between intact and managed forests were also assessed using the two-sided paired *t* test.

All of the aforementioned statistical analyses were performed using Python through pingouin, statsmodels, and scikit-learn packages. Moreover, the two key parameters in all random forest analyses, i.e., the number of decision trees and the minimum samples per leaf node, were set to 100 and 5, respectively.

Supplementary Materials

This PDF file includes:

Figs. S1 to S25
Tables S1 to S7
References

REFERENCES AND NOTES

1. C. M. P. Ozanne, D. Anhuf, S. L. Boulter, M. Keller, R. L. Kitching, C. Körner, F. C. Meinzer, A. W. Mitchell, T. Nakashizuka, P. L. S. Dias, N. E. Stork, S. J. Wright, M. Yoshimura, Biodiversity meets the atmosphere: A global view of forest canopies. *Science* **301**, 183–186 (2003).
2. A. Nakamura, R. L. Kitching, M. Cao, T. J. Creedy, T. M. Fayle, M. Freiberg, C. N. Hewitt, T. Itioka, L. P. Koh, K. Ma, Y. Malhi, A. Mitchell, V. Novotny, C. M. P. Ozanne, L. Song, H. Wang, L. A. Ashton, Forests and their canopies: Achievements and horizons in canopy science. *Trends Ecol. Evol.* **32**, 438–451 (2017).
3. M. Ehbrecht, D. Seidel, P. Annighofer, H. Kreft, M. Kohler, D. C. Zemp, K. Puettmann, R. Nilus, F. Babweteera, K. Willim, M. Stiers, D. Soto, H. J. Boehmer, N. Fisichelli, M. Burnett, G. Juday, S. L. Stephens, C. Ammer, Global patterns and climatic controls of forest structural complexity. *Nat. Commun.* **12**, 519 (2021).
4. E. A. LaRue, R. T. Fahey, B. C. Alveshere, J. W. Atkins, P. Bhatt, B. Buma, A. Chen, S. Cousins, J. M. Elliott, A. J. Elmore, C. R. Hakkenberg, B. S. Hardiman, J. S. Johnson, D. M. Kashian, A. Koirala, M. Papeş, J. B. S. Hilaire, T. D. Surasinghe, J. Zambrano, L. Zhai, S. Fei, A theoretical framework for the ecological role of three-dimensional structural diversity. *Front. Ecol. Environ.* **21**, 4–13 (2023).
5. F. Zellweger, P. De Frenne, J. Lenoir, P. Vangansbeke, K. Verheyen, M. Bernhardt-Römermann, L. Baeten, R. Hédl, I. Berki, J. Brunet, Forest microclimate dynamics drive plant responses to warming. *Science* **368**, 772–775 (2020).
6. J. W. Atkins, R. T. Fahey, B. H. Hardiman, C. M. Gough, Forest canopy structural complexity and light absorption relationships at the subcontinental scale. *J. Geophys. Res. Biogeosci.* **123**, 1387–1405 (2018).
7. L. J. Williams, A. Paquette, J. Cavender-Bares, C. Messier, P. B. Reich, Spatial complementarity in tree crowns explains overyielding in species mixtures. *Nat. Ecol. Evol.* **1**, 63 (2017).
8. A. C. Bennett, N. G. McDowell, C. D. Allen, K. J. Anderson-Teixeira, Larger trees suffer most during drought in forests worldwide. *Nat. Plants.* **1**, 15139 (2015).
9. J. M. Chen, W. Ju, P. Ciais, N. Viovy, R. Liu, Y. Liu, X. Lu, Vegetation structural change since 1981 significantly enhanced the terrestrial carbon sink. *Nat. Commun.* **10**, 4259 (2019).
10. J. Fang, G. Yu, L. Liu, S. Hu, F. S. Chapin, Climate change, human impacts, and carbon sequestration in China. *Proc. Natl. Acad. Sci. U.S.A.* **115**, 4015–4020 (2018).
11. E. A. LaRue, J. A. Knott, G. M. Domke, H. Y. Chen, Q. Guo, M. Hisano, C. Oswalt, S. Oswalt, N. Kong, K. M. Potter, S. Fei, Structural diversity as a reliable and novel predictor for ecosystem productivity. *Front. Ecol. Environ.* **21**, 33–39 (2023).
12. R. T. Fahey, J. W. Atkins, C. M. Gough, B. S. Hardiman, L. E. Nave, J. M. Tallant, K. J. Nadehoffer, C. Vogel, C. M. Scheuermann, E. Stuart-Haëntjens, L. T. Haber, A. T. Fotis, R. Ricart, P. S. Curtis, Defining a spectrum of integrative trait-based vegetation canopy structural types. *Ecol. Lett.* **22**, 2049–2059 (2019).
13. A. P. Allen, J. H. Brown, J. F. Gillooly, Global biodiversity, biochemical kinetics, and the energetic-equivalence rule. *Science* **297**, 1545–1548 (2002).
14. S. Tao, Q. Guo, C. Li, Z. Wang, J. Fang, Global patterns and determinants of forest canopy height. *Ecology* **97**, 3265–3270 (2016).
15. Y. Su, T. Hu, Y. Wang, Y. Li, J. Dai, H. Liu, S. Jin, Q. Ma, J. Wu, L. Liu, J. Fang, Q. Guo, Large-scale geographical variations and climatic controls on crown architecture traits. *J. Geophys. Res. Biogeosci.* **125**, e2019JG005306 (2020).
16. T. Jucker, O. Bouriaud, D. A. Coomes, J. Baltzer, Crown plasticity enables trees to optimize canopy packing in mixed-species forests. *Funct. Ecol.* **29**, 1078–1086 (2015).

17. A. T. Fotis, T. H. Morin, R. T. Fahey, B. S. Hardiman, G. Bohrer, P. S. Curtis, Forest structure in space and time: Biotic and abiotic determinants of canopy complexity and their effects on net primary productivity. *Agric. For. Meteorol.* **250-251**, 181–191 (2018).
18. L. Georgi, M. Kunz, A. Fichtner, K. F. Reich, A. Bienert, H.-G. Maas, G. von Oheimb, Effects of local neighbourhood diversity on crown structure and productivity of individual trees in mature mixed-species forests. *For. Ecosyst.* **8**, 26 (2021).
19. B. S. Hardiman, G. Bohrer, C. M. Gough, C. S. Vogel, P. S. Curtis, The role of canopy structural complexity in wood net primary production of a maturing northern deciduous forest. *Ecology* **92**, 1818–1827 (2011).
20. Q. Ma, Y. Su, C. Niu, Q. Ma, T. Hu, X. Luo, X. Tai, T. Qiu, Y. Zhang, R. C. Bales, L. Liu, M. Kelly, Q. Guo, Tree mortality during long-term droughts is lower in structurally complex forest stands. *Nat. Commun.* **14**, 7467 (2023).
21. L. J. Williams, E. E. Butler, J. Cavender-Bares, A. Stefanski, K. E. Rice, C. Messier, A. Paquette, P. B. Reich, Enhanced light interception and light use efficiency explain overyielding in young tree communities. *Ecol. Lett.* **24**, 996–1006 (2021).
22. S. J. Mitchell, Wind as a natural disturbance agent in forests: A synthesis. *Forestry* **86**, 147–157 (2013).
23. A. Ali, Forest stand structure and functioning: Current knowledge and future challenges. *Ecol. Indic.* **98**, 665–677 (2019).
24. D. J. N. Young, J. T. Stevens, J. M. Earles, J. Moore, A. Ellis, A. L. Jirka, A. M. Latimer, Long-term climate and competition explain forest mortality patterns under extreme drought. *Ecol. Lett.* **20**, 78–86 (2017).
25. X. Yi, N. Wang, H. Ren, J. Yu, T. Hu, Y. Su, X. Mi, Q. Guo, K. Ma, From canopy complementarity to asymmetric competition: The negative relationship between structural diversity and productivity during succession. *J. Ecol.* **110**, 457–465 (2021).
26. X. Liu, Q. Ma, X. Wu, T. Hu, G. Dai, J. Wu, S. Tao, S. Wang, L. Liu, Q. Guo, Y. Su, Nonscalability of fractal dimension to quantify canopy structural complexity from individual trees to forest stands. *J. Remote Sens* **2022**, 0001 (2022).
27. J. W. Atkins, G. Bohrer, R. T. Fahey, B. S. Hardiman, T. H. Morin, A. E. L. Stovall, N. Zimmerman, C. M. Gough, S. Goslee, Quantifying vegetation and canopy structural complexity from terrestrial LiDAR data using the FORESTR R package. *Methods Ecol. Evol.* **9**, 2057–2066 (2018).
28. Q. Guo, Y. Su, T. Hu, H. Guan, S. Jin, J. Zhang, X. Zhao, K. Xu, D. Wei, M. Kelly, N. C. Coops, Lidar boosts 3D ecological observations and modelings: A review and perspective. *IEEE Geosci. Remote Sens. Mag.* **9**, 232–257 (2021).
29. R. Dubayah, J. B. Blair, S. Goetz, L. Fatoyinbo, M. Hansen, S. Healey, M. Hofton, G. Hurtt, J. Kellner, S. Luthcke, The global ecosystem dynamics investigation: High-resolution laser ranging of the Earth's forests and topography. *Sci. Remote Sens.* **1**, 100002 (2020).
30. X. Liu, Q. Ma, X. Wu, T. Hu, Z. Liu, L. Liu, Q. Guo, Y. Su, A novel entropy-based method to quantify forest canopy structural complexity from multiplatform lidar point clouds. *Remote Sens. Environ.* **282**, 113280 (2022).
31. G. Forzieri, V. Dakos, N. G. McDowell, A. Ramdane, A. Cescatti, Emerging signals of declining forest resilience under climate change. *Nature* **608**, 534–539 (2022).
32. D. M. Olson, E. Dinerstein, E. D. Wikramanayake, N. D. Burgess, G. V. Powell, E. C. Underwood, J. A. D'amico, I. Itoua, H. E. Strand, J. C. Morrison, Terrestrial ecoregions of the world: A new map of life on Earth. *Bioscience* **51**, 933–938 (2001).
33. M. Baudena, S. C. Dekker, P. M. Van Bodegom, B. Cuesta, S. I. Higgins, V. Lehsten, C. H. Reick, M. Rietkerk, S. Scheiter, Z. Yin, M. A. Zavala, V. Brovkin, Forests, savannas, and grasslands: Bridging the knowledge gap between ecology and Dynamic Global Vegetation Models. *Biogeosciences* **12**, 1833–1848 (2015).
34. A. Paquette, C. Messier, The effect of biodiversity on tree productivity: From temperate to boreal forests. *Glob. Ecol. Biogeogr.* **20**, 170–180 (2011).
35. A. J. Hansen, P. Burns, J. Ervin, S. J. Goetz, M. Hansen, O. Venter, J. E. M. Watson, P. A. Jantz, A. L. S. Virnig, K. Barnett, R. Pillay, S. Atkinson, C. Supples, S. Rodríguez-Buritica, D. Armenteras, A policy-driven framework for conserving the best of Earth's remaining moist tropical forests. *Nat. Ecol. Evol.* **4**, 1377–1384 (2020).
36. M. C. Hansen, P. V. Potapov, R. Moore, M. Hancher, S. A. Turubanova, A. Tyukavina, D. Thau, S. V. Stehman, S. J. Goetz, T. R. Loveland, A. Kommareddy, A. Egorov, L. Chini, C. O. Justice, J. R. G. Townshend, High-resolution global maps of 21st-century forest cover change. *Science* **342**, 850–853 (2013).
37. L. Poggio, L. M. De Sousa, N. H. Batjes, G. B. M. Heuvelink, B. Kempen, E. Ribeiro, D. Rossiter, SoilGrids 2.0: Producing soil information for the globe with quantified spatial uncertainty. *SOIL* **7**, 217–240 (2021).
38. F. S. Chapin, P. A. Matson, H. A. Mooney, P. M. Vitousek, *Principles of Terrestrial Ecosystem Ecology* (Springer, 2002).
39. D. J. Currie, G. G. Mittelbach, H. V. Cornell, R. Field, J.-F. Guegan, B. A. Hawkins, D. M. Kaufman, J. T. Kerr, T. Oberdorff, E. O'Brien, J. R. G. Turner, Predictions and tests of climate-based hypotheses of broad-scale variation in taxonomic richness. *Ecol. Lett.* **7**, 1121–1134 (2004).
40. C. M. Gough, J. W. Atkins, R. T. Fahey, B. S. Hardiman, High rates of primary production in structurally complex forests. *Ecology* **100**, e02864 (2019).
41. Y. Yu, T. Gao, J. Zhu, X. Wei, Q. Guo, Y. Su, Y. Li, S. Deng, M. Li, Terrestrial laser scanning-derived canopy interception index for predicting rainfall interception. *Ecohydrology* **13**, e2212 (2020).
42. Y. Feng, B. Schmid, M. Loreau, D. I. Forrester, S. Fei, J. Zhu, Z. Tang, J. Zhu, P. Hong, C. Ji, Y. Shi, H. Su, X. Xiong, J. Xiao, S. Wang, J. Fang, Multispecies forest plantations outyield monocultures across a broad range of conditions. *Science* **376**, 865–868 (2022).
43. R. T. Fahey, A. T. Fotis, K. D. Woods, Quantifying canopy complexity and effects on productivity and resilience in late-successional hemlock-hardwood forests. *Ecol. Appl.* **25**, 834–847 (2015).
44. P. R. Moorcroft, G. C. Hurtt, S. W. Pacala, A method for scaling vegetation dynamics: The ecosystem demography model (ED). *Ecol. Monogr.* **71**, 557–586 (2001).
45. A. T. Moles, D. I. Warton, L. Warman, N. G. Swenson, S. W. Laffan, A. E. Zanne, A. Pitman, F. A. Hemmings, M. R. Leishman, Global patterns in plant height. *J. Ecol.* **97**, 923–932 (2009).
46. D. Liu, T. Wang, J. Peñuelas, S. Piao, Drought resistance enhanced by tree species diversity in global forests. *Nat. Geosci.* **15**, 800–804 (2022).
47. T. F. Au, J. T. Maxwell, S. M. Robeson, J. Li, S. M. O. Siani, K. A. Novick, M. P. Dannenberg, R. P. Phillips, T. Li, Z. Chen, J. Lenoir, Younger trees in the upper canopy are more sensitive but also more resilient to drought. *Nat. Clim. Chang.* **12**, 1168–1174 (2022).
48. T. Bohner, J. Diez, Tree resistance and recovery from drought mediated by multiple abiotic and biotic processes across a large geographic gradient. *Sci. Total Environ.* **789**, 147744 (2021).
49. K. Karila, M. Vastaranta, M. Karjalainen, S. Kaasalainen, Tandem-X interferometry in the prediction of forest inventory attributes in managed boreal forests. *Remote Sens. Environ.* **159**, 259–268 (2015).
50. M. Migliavacca, T. Musavi, M. D. Mahecha, J. A. Nelson, J. Knauer, D. D. Baldocchi, O. Perez-Priego, R. Christiansen, J. Peters, K. Anderson, M. Bahn, T. A. Black, P. D. Blanken, D. Bonal, N. Buchmann, S. Caldararu, A. Carrara, N. Carvalhais, A. Cescatti, J. Chen, J. Cleverly, E. Cremonese, A. R. Desai, T. S. El-Madany, M. M. Farella, M. Fernandez-Martinez, G. Filippa, M. Forkel, M. Galvagno, U. Gomarasca, C. M. Gough, M. Gockede, A. Ibrom, H. Ikawa, I. A. Janssens, M. Jung, J. Kattge, T. F. Keenan, A. Knohl, H. Kobayashi, G. Kraemer, B. E. Law, M. J. Liddell, X. Ma, I. Mammarella, D. Martini, C. Macfarlane, G. Matteucci, L. Montagnani, D. E. Pabon-Moreno, C. Panigada, D. Papale, E. Pendall, J. Penuelas, R. P. Phillips, P. B. Reich, M. Rossini, E. Rotenberg, R. L. Scott, C. Stahl, U. Weber, G. Wohlfahrt, S. Wolf, I. J. Wright, D. Yakir, S. Zaehle, M. Reichstein, The three major axes of terrestrial ecosystem function. *Nature* **598**, 468–472 (2021).
51. C. L. Meier, K. M. Thibault, D. T. Barnett, Spatial and temporal sampling strategy connecting NEON Terrestrial Observation System protocols. *Ecosphere* **14**, e4455 (2023).
52. X. Zhao, Q. Guo, Y. Su, B. Xue, Improved progressive TIN densification filtering algorithm for airborne LiDAR data in forested areas. *ISPRS J. Photogramm. Remote Sens.* **117**, 79–91 (2016).
53. Food and Agriculture Organization (FAO), "Global forest resources assessment 2020. Terms and definitions" (FAO, 2018).
54. S. Running, M. Zhao, "MOD17A3HGF MODIS/Terra Net Primary Production Gap-Filled Yearly L4 Global 500 m SIN Grid V061" (US Geological Survey, 2019); http://dx.doi.org/10.5067/MODIS/MOD17A3HGF.061.
55. X. Li, J. Xiao, Mapping photosynthesis solely from solar-induced chlorophyll Fluorescence: A global, fine-resolution dataset of gross primary production derived from OCO-2. *Remote Sens. (Basel)* **11**, 2563 (2019).
56. M. Scheffer, J. Bascompte, W. A. Brock, V. Brovkin, S. R. Carpenter, V. Dakos, H. Held, E. H. van Nes, M. Rietkerk, G. Sugihara, Early-warning signals for critical transitions. *Nature* **461**, 53–59 (2009).
57. Y. Feng, H. Su, Z. Tang, S. Wang, X. Zhao, H. Zhang, C. Ji, J. Zhu, P. Xie, J. Fang, Reduced resilience of terrestrial ecosystems locally is not reflected on a global scale. *Commun. Earth Environ.* **2**, 88 (2021).
58. K. Didan, "MODIS/Terra Vegetation Indices 16-Day L3 Global 1 km SIN Grid V061" (US Geological Survey, 2021); http://dx.doi.org/10.5067/MODIS/MOD13A2.061.
59. W. J. D. Van Leeuwen, A. R. Huete, T. W. Laing, MODIS vegetation index compositing approach. *Remote Sens. Environ.* **69**, 264–280 (1999).
60. J. Liang, J. G. P. Gamarra, N. Picard, M. Zhou, B. Pijanowski, D. F. Jacobs, P. B. Reich, T. W. Crowther, G. J. Nabuurs, S. de-Miguel, J. Fang, C. W. Woodall, J. C. Svenning, T. Jucker, J. F. Bastin, S. K. Wiser, F. Slik, B. Herault, G. Alberti, G. Keppel, G. M. Hengeveld, P. L. Ibisch, C. A. Silva, H. Ter Steege, P. L. Peri, D. A. Coomes, E. B. Searle, K. von Gadow, B. Jaroszewicz, A. O. Abbasi, M. Abegg, Y. C. A. Yao, J. Aguirre-Gutierrez, A. M. A. Zambrano, J. Altman, E. Alvarez-Davila, J. G. Alvarez-Gonzalez, L. F. Alves, B. H. K. Amani, C. A. Amani, C. Ammer, B. A. Ilondea, C. Anton-Fernandez, V. Avitabile, G. A. Aymard, A. F. Azihou, J. A. Baard, T. R. Baker, R. Balazy, M. L. Bastian, R. Batumike, M. Bauters, H. Beeckman, N. M. H. Benu, R. Bitariho, P. Boeckx, J. Bogaert, F. Bongers, O. Bouriaud, P. H. S. Brancalion, S. Brandl, F. Q. Brearley, J. Briseno-Reyes, E. N. Broadbent, H. Bruelheide, E. Bulte, A. C. Catlin, R. C. Gatti, R. G. Cesar, H. Y. H. Chen, C. Chisholm, E. Cienciala, G. D. Colletta, J. J. Corral-Rivas, A. Cuchietti, A. Cuni-Sanchez, J. A. Dar, S. Dayanandan, T. de Haulleville, M. Decuyper, S. Delabye, G. Derroire, B. DeVries, J. Diisi, T. V. Do, J. Dolezal, A. Dourdain,

G. P. Durrheim, N. L. E. Obiang, C. E. N. Ewango, T. J. Eyre, T. M. Fayle, L. F. N. Feunang, L. Finer, M. Fischer, J. Fridman, L. Frizzera, A. L. de Gasper, D. Gianelle, H. B. Glick, M. S. Gonzalez-Elizondo, L. Gorenstein, R. Habonayo, O. J. Hardy, D. J. Harris, A. Hector, A. Hemp, M. Herold, A. Hillers, W. Hubau, T. Ibanez, N. Imai, G. Imani, A. M. Jagodzinski, S. Janecek, V. K. Johannsen, C. A. Joly, B. Jumbam, B. Kabelong, G. A. Kahsay, V. Karminov, K. Kartawinata, J. N. Kassi, E. Kearsley, D. K. Kennard, S. Kepfer-Rojas, M. L. Khan, J. N. Kigomo, H. S. Kim, C. Klauberg, Y. Klomberg, H. Korjus, S. Kothandaraman, F. Kraxner, A. Kumar, R. Kuswandi, M. Lang, M. J. Lawes, R. V. Leite, G. Lentner, S. L. Lewis, M. B. Libalah, J. Lisingo, P. M. Lopez-Serrano, H. Lu, N. V. Lukina, A. M. Lykke, V. Maicher, B. S. Maitner, E. Marcon, A. R. Marshall, E. H. Martin, O. Martynenko, F. M. Mbayu, M. T. E. Mbuvi, J. A. Meave, C. Merow, S. Miscicki, V. S. Moreno, A. Morera, S. A. Mukul, J. C. Muller, A. Murdjoko, M. G. Nava-Miranda, L. E. Ndive, V. J. Neldner, R. V. Nevenic, L. N. Nforbelie, M. L. Ngoh, A. E. N'Guessan, M. R. Ngugi, A. S. K. Ngute, E. N. N. Njila, M. C. Nyako, T. O. Ochuodho, J. Oleksyn, A. Paquette, E. I. Parfenova, M. Park, M. Parren, N. Parthasarathy, S. Pfautsch, O. L. Phillips, M. T. F. Piedade, D. Piotto, M. Pollastrini, L. Poorter, J. R. Poulsen, A. D. Poulsen, H. Pretzsch, M. Rodeghiero, S. G. Rolim, F. Rovero, E. Rutishauser, K. Sagheb-Talebi, P. Saikia, M. N. Sainge, C. Salas-Eljatib, A. Salis, P. Schall, D. Schepaschenko, M. Scherer-Lorenzen, B. Schmid, J. Schongart, V. Seben, G. Sellan, F. Selvi, J. M. Serra-Diaz, D. Sheil, A. Z. Shvidenko, P. Sist, A. F. Souza, K. J. Sterenczak, M. J. P. Sullivan, S. Sundarapandian, M. Svoboda, M. D. Swaine, N. Targhetta, N. Tchebakova, L. A. Trethowan, R. Tropek, J. T. Mukendi, P. M. Umunay, V. A. Usoltsev, G. V. Laurin, R. Valentini, F. Valladares, F. van der Plas, D. J. Vega-Nieva, H. Verbeeck, H. Viana, A. C. Vibrans, S. A. Vieira, J. Vleminckx, C. E. Waite, H. F. Wang, E. K. Wasingya, C. Wekesa, B. Westerlund, F. Wittmann, V. Wortel, T. Zawila-Niedzwiecki, C. Zhang, X. Zhao, J. Zhu, X. Zhu, Z. X. Zhu, I. C. Zo-Bi, C. Hui, Co-limitation towards lower latitudes shapes global forest diversity gradients. *Nat. Ecol. Evol.* **6**, 1423–1437 (2022).
61. S. Fei, I. Jo, Q. Guo, D. A. Wardle, J. Fang, A. Chen, C. M. Oswalt, E. G. Brockerhoff, Impacts of climate on the biodiversity-productivity relationship in natural forests. *Nat. Commun.* **9**, 5436 (2018).
62. S. Besnard, S. Koirala, M. Santoro, U. Weber, J. Nelson, J. Gütter, B. Herault, J. Kassi, A. N'Guessan, C. Neigh, B. Poulter, T. Zhang, N. Carvalhais, Mapping global forest age from forest inventories, biomass and climate data. *Earth Syst. Sci. Data* **13**, 4881–4896 (2021).
63. S. E. Fick, R. J. Hijmans, WorldClim 2: New 1-km spatial resolution climate surfaces for global land areas. *Int. J. Climatol.* **37**, 4302–4315 (2017).
64. R. J. Zomer, J. Xu, A. Trabucco, Version 3 of the global aridity index and potential evapotranspiration database. *Sci. Data* **9**, 409 (2022).
65. H. Tang, J. Stoker, S. Luthcke, J. Armston, K. Lee, B. Blair, M. Hofton, Evaluating and mitigating the impact of systematic geolocation error on canopy height measurement performance of GEDI. *Remote Sens. Environ.* **291**, 113571 (2023).
66. S. Hancock, J. Armston, M. Hofton, X. Sun, H. Tang, L. I. Duncanson, J. R. Kellner, R. Dubayah, The GEDI simulator: A large-footprint waveform lidar simulator for calibration and validation of spaceborne missions. *Earth Space Sci.* **6**, 294–310 (2019).
67. L. Duncanson, J. R. Kellner, J. Armston, R. Dubayah, D. M. Minor, S. Hancock, S. P. Healey, P. L. Patterson, S. Saarela, S. Marselis, C. E. Silva, J. Bruening, S. J. Goetz, H. Tang, M. Hofton, B. Blair, S. Luthcke, L. Fatoyinbo, K. Abernethy, A. Alonso, H.-E. Andersen, P. Aplin, T. R. Baker, N. Barbier, J. F. Bastin, P. Biber, P. Boeckx, J. Bogaert, L. Boschetti, P. B. Boucher, D. S. Boyd, D. F. R. P. Burslem, S. Calvo-Rodriguez, J. Chave, R. L. Chazdon, D. B. Clark, D. A. Clark, W. B. Cohen, D. A. Coomes, P. Corona, K. C. Cushman, M. E. J. Cutler, J. W. Dalling, M. Dalponte, J. Dash, S. de-Miguel, S. Deng, P. W. Ellis, B. Erasmus, P. A. Fekety, A. Fernandez-Landa, A. Ferraz, R. Fischer, A. G. Fisher, A. García-Abril, T. Gobakken, J. M. Hacker, M. Heurich, R. A. Hill, C. Hopkinson, H. Huang, S. P. Hubbell, A. T. Hudak, A. Huth, B. Imbach, K. J. Jeffery, M. Katoh, E. Kearsley, D. Kenfack, N. Kljun, N. Knapp, K. Král, M. Krůček, N. Labrière, S. L. Lewis, M. Longo, R. M. Lucas, R. Main, J. A. Manzanera, R. V. Martínez, R. Mathieu, H. Memiaghe, V. Meyer, A. M. Mendoza, A. Monerris, P. Montesano, F. Morsdorf, E. Næsset, L. Naidoo, R. Nilus, M. O'Brien, D. A. Orwig, K. Papathanassiou, G. Parker, C. Philipson, O. L. Phillips, J. Pisek, J. R. Poulsen, H. Pretzsch, C. Rüdiger, S. Saatchi, A. Sanchez-Azofeifa, N. Sanchez-Lopez, R. Scholes, C. A. Silva, M. Simard, A. Skidmore, K. Stereńczak, M. Tanase, C. Torresan, R. Valbuena, H. Verbeeck, T. Vrska, K. Wessels, J. C. White, L. J. T. White, E. Zahabu, C. Zgraggen, Aboveground biomass density models for NASA's Global Ecosystem Dynamics Investigation (GEDI) lidar mission. *Remote Sens. Environ.* **270**, 112845 (2022).
68. R. Vallat, Pingouin: Statistics in Python. *J. Open Source Soft.* **3**, 1026 (2018).
69. L. Breiman, Random forests. *Mach. Learn.* **45**, 5–32 (2001).
70. S. Seabold, J. Perktold, "Statsmodels: Econometric and statistical modeling with Python" in *Proceedings of the 9th Python in Science Conference* (2010), pp. 92–96.
71. F. Pedregosa, G. Varoquaux, A. Gramfort, V. Michel, B. Thirion, O. Grisel, M. Blondel, P. Prettenhofer, R. Weiss, V. Dubourg, Scikit-learn: Machine learning in Python. *J. Mach. Learn. Res.* **12**, 2825–2830 (2011).
72. P. Potapov, M. C. Hansen, L. Laestadius, S. Turubanova, A. Yaroshenko, C. Thies, W. Smith, I. Zhuravleva, A. Komarova, S. Minnemeyer, E. Esipova, The last frontiers of wilderness: Tracking loss of intact forest landscapes from 2000 to 2013. *Sci. Adv.* **3**, e1600821 (2017).
73. J. M. Andrade, M. G. Estévez-Pérez, Statistical comparison of the slopes of two regression lines: A tutorial. *Anal. Chim. Acta* **838**, 1–12 (2014).
74. K. A. Novick, J. A. Biederman, A. R. Desai, M. E. Litvak, D. J. P. Moore, R. L. Scott, M. S. Torn, The AmeriFlux network: A coalition of the willing. *Agric. For. Meteorol.* **249**, 444–456 (2018).

Acknowledgments: We thank the forest ecosystem research stations at Dongling Mountain, Shennongjia, and Gutian Mountain for data support and all other sources of freely accessible data used in this study. **Funding:** This work was supported by the National Key R&D Program of China, 2022YFF0803100 (Y.S.); the National Natural Science Foundation of China, 32271640 (T.H.) and 31922090 (J.W.); the Hong Kong Research Grant Council Collaborative Research Fund, C5062-21GF (J.W.); and the Innovation and Technology Fund (funding support to State Key Laboratories in Hong Kong of Agrobiotechnology) of the HKSAR, China (J.W.). **Author contributions:** Conceptualization: Y.S. and X.L. Methodology: X.L., Y.S., Y.F., and Y.L. Investigation: X.L. and Y.S. Visualization: X.L., Y.S., and L.L. Funding acquisition: Y.S., T.H., and J.W. Project administration: Y.S. Supervision: Y.S. Writing—original draft: X.L. and Y.S. Writing—review and editing: All authors. **Competing interests:** The authors declare that they have no competing interests. **Data and materials availability:** All data needed to evaluate the conclusions in the paper are present in the paper and/or the Supplementary Materials. Data and code supporting the findings of this study are accessible on Figshare (DOI: 10.6084/m9.figshare.25047371). All public datasets used in the current study are appropriately cited and openly accessible (see table S1).

Submitted 4 October 2023
Accepted 12 April 2024
Published 15 May 2024
10.1126/sciadv.adl1947